Tokamap: A Hamiltonian twist map for magnetic field lines in a toroidal geometry

R. Balescu, M. Vlad,* and F. Spineanu*
Association Euratom–Etat Belge, Code Postal 231, Université Libre de Bruxelles, Campus Plaine, Boulevard du Triomphe, 1050 Bruxelles, Belgium

(Received 27 January 1998; revised manuscript received 25 March 1998)

A Hamiltonian twist map (tokamap) is constructed as a representation of the stroboscopic plot of magnetic field lines in a toroidal confinement device as used in fusion physics. This ''tokamap'' is compatible with minimal toroidal geometry requirements (in particular, the polar axis cannot be crossed upon iteration). It depends on two parameters: the stochasticity parameter K and the winding number on axis, w. With increasing values of K, chaotic regions appear mostly near the edge of the torus, while the zone near the magnetic axis remains very robust. The number and nature of the fixed points are studied in detail, as they determine the appearance of the phase portraits near the axis. It is shown that the topology undergoes several bifurcations as K and/or w are varied. The various phase portraits reproduce the qualitative features known in tokamak physics. The time series exhibit a typical behavior describable by a continuous time random walk, as found in previous works on the standard map. [S1063-651X(98)05607-4]

PACS number(s): 52.55.Fa, 05.45.+b, 52.25.Gj, 05.40.+j

I. INTRODUCTION

Magnetic confinement of a plasma (for the purpose of controlled thermonuclear fusion) is realized in tokamaks or stellarators by a magnetic field ideally structured by a set of nested toroidal *magnetic surfaces* wound around a circular *magnetic axis*. The successive surfaces are labeled by the values of any *surface quantity* (i.e., a quantity that is constant on a magnetic surface) Ψ, playing the role of a radial coordinate. Each magnetic field line is tangent everywhere to a magnetic surface. Any point on such a surface is characterized by two angular coordinates: the poloidal angle θ (the short way around the torus) and the toroidal angle ζ (the long way around the torus): for convenience these angles are measured in radians divided by 2π.

To put the matter into quantitative form, we consider first an *ideal (unperturbed) situation* [1]. We choose here for the radial coordinate Ψ the *toroidal flux* $\tilde{\psi}$, i.e., the magnetic flux through a surface perpendicular to the magnetic axis; for convenience, this quantity is made dimensionless by introducing $\psi=\tilde{\psi}/B_0a^2$, where B_0 is a characteristic magnetic field amplitude, and a is the minor radius of the tokamak. In the case of a circular torus, we have simply $\psi=r^2$, where r is the dimensionless radial coordinate (scaled with a). The magnetic axis thus corresponds to the value $\psi=0$, and the edge of the torus to $\psi=1$. The variables (ψ,θ,ζ) form a convenient curvilinear coordinate system, that can be made orthogonal by a proper choice of the angles.

The (stationary) magnetic field $\mathbf{B}(\mathbf{x})$ must satisfy the two constraints expressing its divergence-free nature, and its tangency to the magnetic surface $\psi(\mathbf{x})=\text{const}$:

$$\nabla\cdot\mathbf{B}=0, \quad \mathbf{B}\cdot\nabla\psi=0. \tag{1}$$

The magnetic field satisfying these constraints is conveniently represented in the well-known *Clebsch form* [1–3]:

$$\mathbf{B}=\nabla\psi\times\nabla\theta-\nabla\alpha_0(\psi)\cdot\nabla\zeta, \tag{2}$$

where the surface quantity $\alpha_0(\psi)$ is the (dimensionless) *poloidal flux* (the magnetic field and the gradient operators are also made dimensionless by scaling them with B_0 and a, respectively).

From Eq. (2), one finds the equations for the magnetic field lines expressed in the coordinates (ψ,θ,ζ) by using elementary geometrical formulas. Using the toroidal angle as a running parameter, a field line is characterized by the two functions $\psi(\zeta)$ and $\theta(\zeta)$ obeying the following differential equations:

$$\frac{d\psi}{d\zeta}=-\frac{\partial\alpha_0}{\partial\theta}, \quad \frac{d\theta}{d\zeta}=\frac{\partial\alpha_0}{\partial\psi}. \tag{3}$$

As noted by many authors (e.g., Refs. [4–8]), the field line equations have a *Hamiltonian structure*: α_0 plays the role of the Hamiltonian, ζ the role of ''time,'' and ψ and θ appear as a pair of canonical variables (this property justifies the choice of ψ as a radial coordinate). In the unperturbed case, when α_0 is a surface quantity depending only on ψ, Eqs. (3) represent a one degree of freedom, hence integrable, dynamical system:

$$\frac{d\psi}{d\zeta}=0, \quad \frac{d\theta}{d\zeta}=W(\psi), \tag{4}$$

where the unperturbed *winding number* (also called the *rotational transform*) is defined as follows:

$$W(\psi)=\frac{\partial\alpha_0(\psi)}{\partial\psi}. \tag{5}$$

(In the plasma physics literature, this quantity is often denoted by $\iota/2\pi$; its inverse $q=1/W$ is called the *safety fac-*

*Permanent address: National Institute for Laser, Plasma and Radiation Physics, P.O. Box MG-36, Magurele, Bucharest, Romania.

 © 1998 The American Physical Society

tor). Clearly, ψ is analogous to an action variable, a constant of the motion; the associated angle variable increases linearly in time.

This ideal structure is, however, strongly modified whenever some perturbation is present: the latter can be due to external features (such as imperfections in the coils producing the magnetic field) or to internal factors (i.e., instabilities or fluctuations). The *perturbed magnetic field* is also conveniently represented in the Clebsch form (2), in which the unperturbed Hamiltonian is replaced by a function of all three coordinates:

$$\alpha_0 \rightarrow \alpha = \alpha_0(\psi) + K\delta\alpha(\psi,\theta,\zeta). \tag{6}$$

The perturbation Hamiltonian $K\delta\alpha$ is a 1-periodic function of the variables θ and ζ. The real, positive parameter K, is called the *stochasticity parameter*: it measures the strength of the perturbation. The corresponding equations of the field lines are now

$$\frac{d\psi}{d\zeta} = -K\,\frac{\partial\delta\alpha(\psi,\theta,\zeta)}{\partial\theta},$$
$$\frac{d\theta}{d\zeta} = W(\psi) + K\,\frac{\partial\delta\alpha(\psi,\theta,\zeta)}{\partial\psi}. \tag{7}$$

These are the equations of motion of a $1\frac{1}{2}$ degrees of freedom dynamical system, which is, generically, nonintegrable. The nature of the orbits is conveniently studied by considering a stroboscopic plot, obtained by recording the values of the coordinates (ψ,θ) at successive equal times. These coordinates define the *phase space* of the dynamical system. For simplicity, we assume the cross section of the torus to be circular. The stroboscopic plot of the *unperturbed* system consists of a set of concentric circles (corresponding to ergodic magnetic surfaces) interspersed with discrete points (corresponding to rational values of the winding number). The stroboscopic plot coincides in this case with a Poincaré section on a plane perpendicular to the magnetic axis. An alternative graphical representation, which often provides a clearer picture, is obtained by making a cut starting from the center (magnetic axis), pulling the two lips apart, and expanding the point representing the magnetic axis into a line; after a mirror reflection we obtain a square diagram; the radial coordinate ψ is represented on the vertical axis $(0 \leqslant \psi \leqslant 1)$, and the poloidal angle is given, modulo 1, on the horizontal axis $(0 \leqslant \theta \leqslant 1)$ (Fig. 1). The ergodic magnetic surfaces are now represented as horizontal segments, and the periodic orbits are shown as points aligned horizontally. Whenever a *perturbation* is present, the topology of the magnetic field is strongly modified: there appear *island chains*, together with undestroyed (but deformed) magnetic surfaces called *Kolmogorov-Arnold-Moser (KAM) barriers* and in between these features there exist *chaotic orbits* filling two-dimensional regions of the phase space. This *incompletely chaotic structure* is generic for tokamaks; its understanding is a prerequisite for any realistic study of transport in such devices. The peculiar features connected with the representation of the magnetic axis will be discussed in Sec. V.

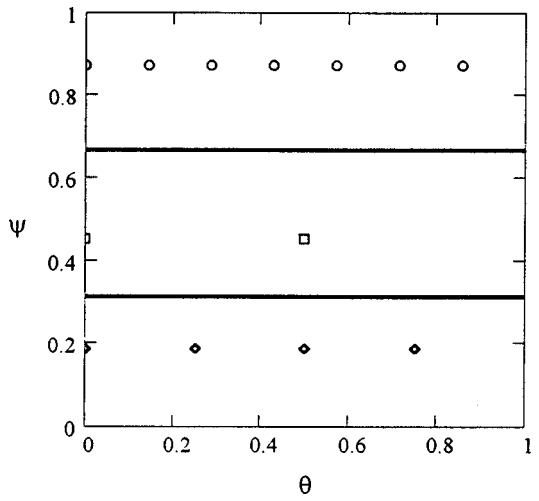

FIG. 1. Phase portrait of unperturbed system (square representation).

II. CONSTRUCTION OF THE TOKAMAP

The solution of the field line equations (7) required for the construction of the stroboscopic plot involves a very heavy numerical effort for achieving sufficient precision in the nonintegrable case [9–11]. It is therefore useful to construct simplified models based on discrete iterative *maps* rather than on differential equations in order to describe the stroboscopic plot of the magnetic field. With this mathematical tool, very long orbits are easily obtained even with a modest personal computer. It is generally not a simple matter to construct a map that is *exactly* equivalent to the starting differential equations (this would imply the solution of the latter, which is precisely what we want to avoid). One may wish to construct, instead, a model *ab initio*, and check its relevance *a posteriori*.

Several authors have introduced maps representing various aspects of magnetic confinement devices according to this philosophy. The first application of a Hamiltonian map to the problem of magnetic field line diffusion in a tokamak (in presence of a magnetic limiter) appears to be due to Martin and Taylor in 1984 [12]. Punjabi and co-workers [13–15] studied the X point in a poloidal divertor geometry of a tokamak by means of very simple algebraic maps. Abdullaev and Zaslavsky studied the same divertor problem by means of a more sophisticated ''separatrix map'' [16,17]. Abdullaev *et al.* recently constructed a map representing the effect of a dynamic ergodic divertor [18]. All these works are models of the edge region (scrape-off layer) of a tokamak. A global model of a specific stellarator (W VII-A) was introduced by Wobig in an important work [8] (see also Ref. [19]).

In the present work, we construct a global model of the magnetic field in a toroidal confinement device by means of an *iterative two-dimensional* (ψ,θ) *map*. Such a map connects successive iterates of the phase-space coordinates as follows:

$$\psi_{\nu+1} = P(\psi_\nu,\theta_\nu), \quad \theta_{\nu+1} = \Theta(\psi_\nu,\theta_\nu), \tag{8}$$

where ν is any non-negative integer: $\nu = 0,1,2,\ldots$. The construction of such a map must satisfy a certain number of

constraints. The first of these requires that the *Hamiltonian structure* of the differential equations (7) be reflected in the structure of the discrete model, which should be a *Hamiltonian* (or *symplectic*) map. The clearest way of constructing such a map starts from the fact [20] that in a Hamiltonian evolution the values of the canonical variables $\{\psi_{\nu+1},\theta_{\nu+1}\}$ at time $(\nu+1)$ are connected to their values $\{\psi_\nu,\theta_\nu\}$ at time ν by a *canonical transformation*. Such a transformation can be defined by means of a *generating function* of the new momentum and of the old angle [8]:

$$F(\psi_{\nu+1},\theta_\nu)=\psi_{\nu+1}\theta_\nu+f(\psi_{\nu+1},\theta_\nu). \tag{9}$$

The first term in the right hand side corresponds to the identity transformation. The transformation equations are

$$\psi_\nu=\frac{\partial F(\psi_{\nu+1},\theta_\nu)}{\partial\theta_\nu}=\psi_{\nu+1}+\frac{\partial f(\psi_{\nu+1},\theta_\nu)}{\partial\theta_\nu},$$

$$\theta_{\nu+1}=\frac{\partial F(\psi_{\nu+1},\theta_\nu)}{\partial\psi_{\nu+1}}=\theta_\nu+\frac{\partial f(\psi_{\nu+1},\theta_\nu)}{\partial\psi_{\nu+1}}\ (\mathrm{mod}\ 1). \tag{10}$$

These equations define the map in a semi-implicit form (the explicit form is obtained by solving the first equation for $\psi_{\nu+1}$). The *unperturbed map* is obtained by taking $f(\psi_{\nu+1},\theta_\nu)=F_0(\psi_{\nu+1})$. We then obtain

$$\psi_{\nu+1}=\psi_\nu,\quad \theta_{\nu+1}=\theta_\nu+W(\psi_{\nu+1})\ (\mathrm{mod}\ 1). \tag{11}$$

This map represents the exact solution of the integrable Hamiltonian system (4). Indeed, ψ_ν remains constant and θ_ν increases by $W(\psi)$ upon each iteration (i.e., after a toroidal turn of 2π). The winding number is simply related to the generating function

$$W(\psi)=\frac{\partial F_0(\psi)}{\partial\psi}. \tag{12}$$

Comparing this equation to Eq. (5), we see that the generating function is here simply the Hamiltonian of the (continuous time) dynamical system. The phase portrait of this map is of the type shown in Fig. 1. For all the values of ψ such that $W(\psi)=n/p(n,p\in\mathbb{Z})$, the pth iterate coincides (modulo 1) with the starting point, i.e., we have a p-periodic orbit represented by a chain of p discrete points. For all irrational values of W the orbit fills densely a horizontal segment in Fig. 1 (i.e., a circle around the origin in the polar representation). The location of these features depends, of course, on the shape of the winding number function $W(\psi)$. Whenever this is a monotonous (growing or decreasing) function, Eq. (11) is called a *simple twist map*.

We now introduce a *perturbation* by considering a generating function of the form

$$F(\psi_{\nu+1},\theta_\nu)=\psi_{\nu+1}\theta_\nu+F_0(\psi_{\nu+1})+K\delta F(\psi_{\nu+1},\theta_\nu), \tag{13}$$

where K is the stochasticity parameter introduced in Eq. (6). Map (11) becomes

$$\psi_{\nu+1}=\psi_\nu+Kh(\psi_{\nu+1},\theta_\nu),$$

$$\theta_{\nu+1}=\theta_\nu+W(\psi_{\nu+1})+Kj(\psi_{\nu+1},\theta_\nu). \tag{14}$$

From Eq. (10), we find the following definitions:

$$h(\psi_{\nu+1},\theta_\nu)=-\frac{\partial\delta F(\psi_{\nu+1},\theta_\nu)}{\partial\theta_\nu},$$

$$j(\psi_{\nu+1},\theta_\nu)=\frac{\partial\delta F(\psi_{\nu+1},\theta_\nu)}{\partial\psi_{\nu+1}}. \tag{15}$$

It follows that

$$\frac{\partial h(\psi_{\nu+1},\theta_\nu)}{\partial\psi_{\nu+1}}+\frac{\partial j(\psi_{\nu+1},\theta_\nu)}{\partial\theta_\nu}=0. \tag{16}$$

Equations (14), with the functions h and j interrelated by Eq. (16), is the general form of a *Hamiltonian map*. The simple relation between the generating function and Hamiltonian is, however, no longer valid. Generically, whenever the generating function depends *nonadditively* on both ψ and θ, it is not possible to determine the Hamiltonian function that produces a given Hamiltonian map (although the existence of the former is ensured by the construction).

A simple realization of constraint (16) is obtained by taking $h=h(\theta_\nu)$, $j=j(\psi_{\nu+1})$: this corresponds to a *general twist map*. The fact that each function depends on a single variable greatly simplifies the analysis: the maps studied in most textbooks are of this type. In particular, the celebrated *Chirikov-Taylor standard map* [22,21,23] [$h(\theta)=-(2\pi)^{-1}\sin 2\pi\theta$ and $j(\psi)\equiv 0$; $W(\psi)=\psi$] belongs to this class. The standard map is, however, *not a faithful model of a tokamak*, for several reasons. In the first place, the safety factor profile $q(r)$ is, in most tokamak experiments, a monotonously growing function of r, hence of $\psi=r^2$. [In recent experiments one produces a locally ''*reversed shear*,'' i.e., a minimum of $q(r)$ near the magnetic axis. This reversed shear configuration can easily be implemented in our work, and will be discussed in a forthcoming paper]. Typically, the safety factor on the magnetic axis is $q(0)=1$, and, at the edge, $q(1)=4$. The value on axis may, however, be smaller $q(0)<1$: this has an important effect on the properties of the discharge. It follows that in a tokamak *the winding number $W(\psi)$ is a monotonously decreasing function of ψ*: This is just opposite of the standard map.

A useful analytic form for this profile was derived by Misguich and Weyssow [24], by assuming that the density and electron temperature profiles in the tokamak are, respectively, $n(r)=n(0)[1-r^2]$ and $T_e(r)=T_e(0)[1-r^2]^2$; one then obtains, in the large aspect ratio limit,

$$W(\psi)=\frac{w}{4}(2-\psi)(2-2\psi+\psi^2). \tag{17}$$

Here the positive constant $w=W(0)$ is the value of the winding number on the polar axis. The winding number profile $W(\psi)$, given by Eq. (17), as well as the corresponding safety factor $q(\psi)$, are shown in Fig. 2.

A very important additional constraint to be fulfilled by a tokamak model is its *compatibility with toroidal geometry*. It

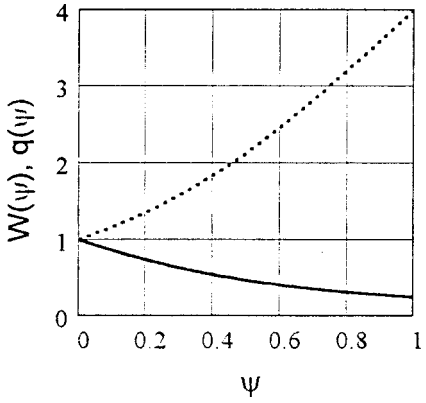

FIG. 2. Usual winding number (solid) and safety factor (dotted) profiles in a tokamak.

follows from its geometrical meaning that the coordinate ψ *must be a definite positive number*; it may vary in the physical range $0 \leqslant \psi \leqslant 1$ (it is bounded by the limiter or the wall; the upper limit is, however, left free in the present model). An indispensable condition is thus

$$\text{If } \psi_0 > 0 \quad \text{then } \psi_\nu > 0, \quad \forall \nu. \tag{18}$$

On the other hand, the polar axis represented by $\psi = 0$ plays a special (singular) role in the toroidal (or cylindrical) geometry. As the radial coordinate can admit no negative values, the axis $\psi = 0$ represents [in the ''square'' representation (Fig. 1)] a barrier that can never be crossed. This condition can be satisfied when the polar axis is globally invariant: an orbit starting on the axis remains forever on the axis:

$$\text{If } \psi_0 = 0 \quad \text{then } \psi_\nu = 0, \quad \forall \nu. \tag{19}$$

The condition of impenetrability can, however, also be realized more weakly, by requiring that a point starting on the axis may either remain on the axis or move to a positive ψ (but never to a negative ψ), thus

$$\text{If } \psi_0 = 0, \quad \text{then } \psi_\nu \geqslant 0, \quad \forall \nu. \tag{20}$$

The standard map does not satisfy any of these conditions. It is well known that, for $K > 0$, an orbit starting at $\psi_0 = 0$ travels through both positive and negative values of ψ. Moreover, (in the globally chaotic regime), the orbits are 1-periodic in ψ (as well as in θ), hence $\psi = 0$ plays no special role: there is no unique polar axis in the standard map.

Wobig [8] took a first step toward solving the problem posed by the geometrical constraints by making the following ansatz for the generating function in Eq. (13): $\delta F(\psi_{\nu+1}, \theta_\nu) = -(2\pi)^{-2} \psi_{\nu+1} \cos 2\pi\theta_\nu$; using Eqs. (14) and (15) he obtained:

$$\psi_{\nu+1} = \psi_\nu - \frac{K}{2\pi} \psi_{\nu+1} \sin 2\pi\theta_\nu, \tag{21}$$

$$\theta_{\nu+1} = \theta_\nu + W(\psi_{\nu+1}) - \frac{K}{(2\pi)^2} \cos 2\pi\theta_\nu.$$

(Actually, Wobig used more general periodic functions of θ_ν; this does not change our forthcoming argument.) Wobig's map satisfies condition (19); however, it violates condition (18) in a certain domain, and may even become singular.

Here we propose an alternative ansatz for the generating function:

$$\delta F(\psi_{\nu+1}, \theta_\nu) = -\frac{1}{(2\pi)^2} \frac{\psi_{\nu+1}}{1+\psi_{\nu+1}} \cos 2\pi\theta_\nu, \tag{22}$$

which yields the following map:

$$\psi_{\nu+1} = \psi_\nu - \frac{K}{2\pi} \frac{\psi_{\nu+1}}{1+\psi_{\nu+1}} \sin 2\pi\theta_\nu, \tag{23}$$

$$\theta_{\nu+1} = \theta_\nu + W(\psi_{\nu+1}) - \frac{K}{(2\pi)^2} \frac{1}{(1+\psi_{\nu+1})^2} \cos 2\pi\theta_\nu. \tag{24}$$

It is readily verified that this map satisfy conditions (16), hence it is a Hamiltonian, area-preserving map. The denominators $(1+\psi_{\nu+1})$ produce a ''self-healing'' effect which suppresses the divergences. The winding number profile considered here will be the one defined in Eq. (17), which depends on the parameter w. It is clear, however, that the shape of $W(\psi)$ should be considered as being open to variation for studying different regimes [just as in real experiments, the shape of the safety factor profile $q(r)$ can be ''tailored''].

In form (23), the map is nonlinear; it possesses two solutions $\psi_{\nu+1}$ for given (ψ_ν, θ_ν). We make the following choice of the unique root which provides us with the final definition of our map:

$$\psi_{\nu+1} = \tfrac{1}{2}\{P(\psi_\nu, \theta_\nu) + \sqrt{[P(\psi_\nu, \theta_\nu)]^2 + 4\psi_\nu}\}, \tag{25}$$

where the function $P(\psi, \theta)$ is defined as

$$P(\psi, \theta) = \psi - 1 - \frac{K}{2\pi} \sin 2\pi\theta. \tag{26}$$

Equations (24)–(26) define a one-valued iterative map which will be called the tokamap.

It is easily checked that condition (18) is satisfied. Indeed, if $\psi > 0$, then $P^2 + 4\psi > P^2$. If $P > 0$, trivially, $P + \sqrt{P^2+4\psi} > 0$. If $P < 0$, we still have $\sqrt{P^2+4\psi} > |P|$, and hence always $P + \sqrt{P^2+4\psi} > 0$.

We now discuss the properties related to the polar axis. From Eq. (26), it is seen that, for $\psi = 0$, the sign of the function $P(0,\theta)$ depends on the value of the stochasticity parameter and on the poloidal angle.

For $(K/2\pi) < 1$, $P(0,\theta) < 0$; thus $P(0,\theta) + \sqrt{P^2(0,\theta)} = 0$, and Eq. (25) shows that $\psi_\nu = 0$ implies $\psi_{\nu+1} = 0$. The polar axis is thus globally invariant in this case, i.e., Eq. (19) is satisfied.

For $(K/2\pi) > 1$, $P(0,\theta)$ is no longer everywhere definite negative: there exists a range of θ for which $P(0,\theta) + \sqrt{P^2(0,\theta)} > 0$, and hence the polar axis is no longer globally invariant in this region. Nevertheless, as shown above,

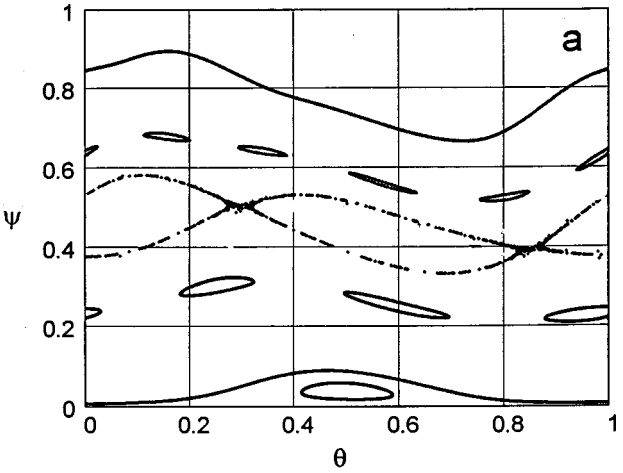

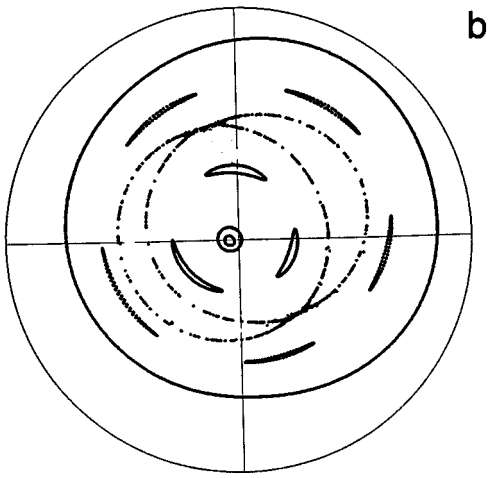

FIG. 3. Tokamap island chains and KAM barriers. ($K=2.55$, the number of iterations is $N=1000$.)

ψ_ν ($\nu>0$) is always positive; in particular, an orbit starting at $\psi_0=0$ can only move to positive values of ψ (or remain on the axis). Hence in this range of K, Eq. (20) is satisfied: *the polar axis cannot be crossed.*

It may be noted that the value $K=2\pi=6.283\ldots$ corresponds to a regime of global chaos for the tokamap. As a result the invariance of the polar axis is no longer a very significant property in this case. Summing up, *the tokamap is a Hamiltonian map, depending on two parameters (K and w), under which an initially positive radial coordinate ψ remains always positive, and the polar axis is a barrier that cannot be crossed.*

III. PHASE PORTRAITS OF THE TOKAMAP

In Fig. 3, we show a typical phase portrait, corresponding to five orbits with $K=2.55$ ($w=1$). We see four island chains around periodic orbits corresponding to winding numbers $W=1$, $\frac{2}{3}$, $\frac{1}{2}$, and $\frac{2}{5}$, as well as two KAM barriers. In the polar plot, the islands are represented as closed curves that do not encircle the origin, whereas the KAM barriers are curves enclosing the origin. The separatrix enclosing the $W=\frac{1}{2}$ island chain is also visible, thus displaying the two hyperbolic (X) points associated with the two elliptic (O) points located at the center of the islands. The increased density of points near the X points shows the beginning of a thin stochastic layer.

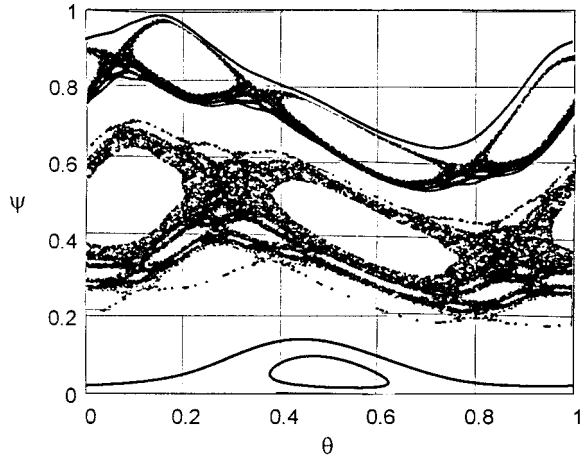

FIG. 4. Tokamap regular and chaotic orbits ($K=3.7$, $w=1$, and $N=10^4$).

In Fig. 4, we take a higher value of $K=3.7$ ($w=1$), and picture five orbits. The remarkable feature here is that the outer part of the torus (near the edge) is now strongly chaotic around the $W=\frac{1}{2}$ and $\frac{1}{3}$ island chains. It is, however, remarkable that *the inner part, near the magnetic axis, remains very robust and undestroyed.* This feature may lead to a model of a tokamap with an ergodic divertor.

An interesting case is shown in Fig. 5. It shows four orbits, for $K=4.5$ ($w=1$). The middle section is strongly chaotic at this value of K; it forms a single ''stochastic belt'' which surrounds several large island chains. This zone is clearly bounded, both below and above, by KAM surfaces, two of which are shown in the figure. The presence of these intact KAM barriers shows that, at this value of the parameter K, the system is *not yet* in a *globally stochastic* regime.

We now recall a well-known semiempirical result of Greene [25], later developed by a renormalization group analysis [26–28]. It states that the most robust KAM barrier in the *standard map* is the one corresponding to a winding number equal to $g_*=G_*^{-1}$, where G_* is the golden section defined by the equation: $G_*^2=G_*+1$ (thus $g_*=G_*-1=0.618\,033\,9\ldots$): this KAM surface will be called ''*the golden KAM.*'' This result is very appealing because, in a

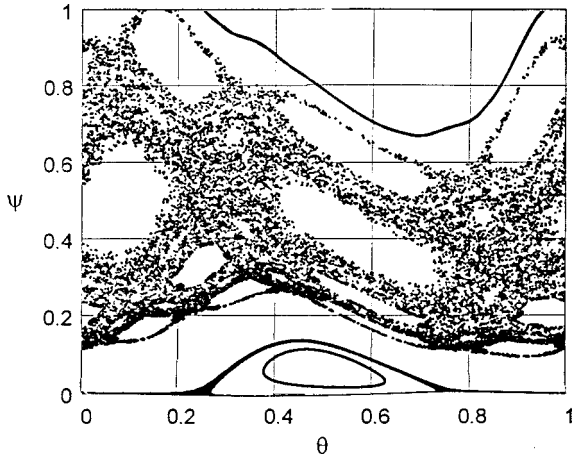

FIG. 5. Tokamap stochastic belt ($K=4.5$, $w=1$, and $N=1.5\times10^4$).

sense, the golden section may qualify as ''the most irrational number,'' being defined as the continued fraction: [1,1,1,1, . . .]. Greene's result is, unfortunately, not generic. The determination of the most robust KAM barrier in an arbitrary map appears to be, at present, a largely unsolved problem [29].

Coming back to the tokamap, we may try to locate the golden KAM in a picture like Fig. 5. For a rather large value of K, it is impossible to ascertain the value of the winding number of a chaotic orbit. We may argue, however, as follows. Consider first the *unperturbed map* ($K=0$). In this case the KAM barriers are represented by horizontal straight segments. The radial coordinate ψ corresponding to any given value of W is determined from the graph of Fig. 2. Alternatively, we can find this number analytically, by solving the cubic equation

$$W(\psi)=\omega, \tag{27}$$

where ω is a given value of the winding number. The real root of Eq. (27) is

$$\psi=J^{1/3}-\frac{2}{9J^{1/3}}+\frac{4}{3}, \tag{28}$$

with

$$J=\tfrac{10}{27}-2\omega+\tfrac{2}{9}\sqrt{3-30\omega+81\omega^2}. \tag{29}$$

We thus find that the golden KAM, with $\omega=g_*\approx 0.618\,03$, is located at $\psi\approx 0.315\,93$. In the same way, we find that the periodic orbit corresponding to $\omega=1/2$ is located at $\psi\approx 0.456\,31$, i.e., *above* the golden KAM, and that the periodic orbit with $\omega=\frac{3}{4}$ lies at $\psi\approx 0.189\,46$, i.e., *below* the golden KAM. The golden KAM, together with these two periodic orbits, is shown in Fig. 1 for the unperturbed tokamap.

Consider now the *perturbed tokamap*, $K>0$. The KAM barriers are no longer straight, but are deformed or broken; on the other hand, islands are formed around the periodic orbits. In spite of these deformations, the general topology of the phase portrait is maintained, in the sense that the *relative* position of the features associated with successive values of the winding number is preserved. In particular, the golden KAM (if it exists) must be located somewhere between the two-island chain ($\omega=\frac{1}{2}$) and the four-island chain ($\omega=\frac{3}{4}$). Looking now at Fig. 5, we clearly recognize these two island chains; in between them there is a purely chaotic sea. Thus, at $K=4.3$, *the golden KAM is destroyed*. On the other hand, the chaotic belt is bounded both above and below by undestroyed KAM barriers. Thus, as noted above, the system is not yet in a globally chaotic state, although the golden KAM is broken. We thus arrive at the following interesting conclusion: *In the tokamap, the golden KAM is not the most robust KAM barrier*. The search for the most resistant barrier is certainly not a trivial matter. It will not be discussed further here.

IV. FIXED POINTS OF THE TOKAMAP

It is seen, especially in Fig. 3, that all island chains of period $p\geqslant 2$ have the ''expected'' structure predicted by the Poincaré-Birkhoff theorem [21,23], which tells us that, whenever $W(\psi)$ is a monotonous function (i.e., for any twist map), a rational surface breaks under a sufficiently small perturbation into an even number $2n$ of fixed points, n elliptic points alternating with n hyperbolic ones. This structure is not apparent for the period-1 fixed O point appearing in Figs. 3 and 4; no corresponding X point is visible. A careful analysis of the proof shows that the breakdown of the theorem is due to the special nature of the polar axis $\psi=0$: the latter cannot be crossed upon iteration by the map. More generally speaking, it will be shown that the phase portrait in the neighborhood of the polar axis is determined by the number and the nature of the fixed points. The latter depend on the relative values of the parameters w and K, and will be analyzed below.

In order to study the problem quantitatively, we write down the equations determining the fixed points by using Eqs. (23) and (24) with $\psi_{\nu+1}=\psi_\nu=\psi$ and $\theta_{\nu+1}=\theta_\nu=\theta$:

$$\frac{\psi}{1+\psi}\sin 2\pi\theta=0, \tag{30}$$

$$W(\psi)-\frac{KA}{(2\pi)^2}\frac{1}{(1+\psi)^2}\cos 2\pi\theta=0 \pmod 1. \tag{31}$$

[In Eq. (30), we used the implicit form of map (23); it should be kept in mind, however, that only one branch of the expression in the right hand side is retained.] The study of fixed points should be completed by a *linear stability* analysis, starting from the tangent map (which we do not write down explicitly here). It has been well known, since the classical work of Refs. [25, 21, 23], that a very simple stability criterion is based on the *residue*, defined as follows in terms of the trace of the matrix M defining the latter map:

$$R=\tfrac{1}{4}(2-\mathrm{Tr}\mathsf{M}). \tag{32}$$

The fixed point (around which the map is linearized) is linearly stable whenever $0\leqslant R\leqslant 1$. The residue for the tokamap is obtained by a standard calculation:

$$\begin{aligned}R=-\frac{K}{8\pi}\Bigg\{&\left[\frac{1}{(1+\psi)^2}-\frac{2\pi}{2\pi(1+\psi)^2+K\sin 2\pi\theta}\right]\sin 2\pi\theta\\&-\frac{K}{\pi}\frac{\psi}{(1+\psi)^4}\cos^2 2\pi\theta\\&+w\,\frac{\pi}{2}\frac{\psi(6-8\psi+3\psi^2)}{1+\psi}\cos 2\pi\theta\Bigg\},\end{aligned} \tag{33}$$

where ψ and θ are the coordinates of the fixed point around which the linearization is made. We recall that the *physical domain of the variables* is $0\leqslant\psi\leqslant 1$, and $0\leqslant\theta\leqslant 1$ (mod 1); the *physical range of the stochasticity parameter* is $0\leqslant K\leqslant 2\pi$.

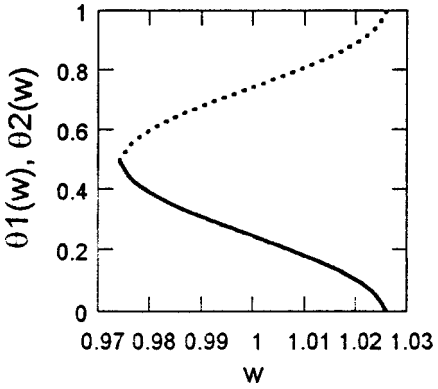

FIG. 6. Angular position of the fixed points on the polar axis ($K=1$). Solid line: $\theta 1$; dotted line: $\theta 2$.

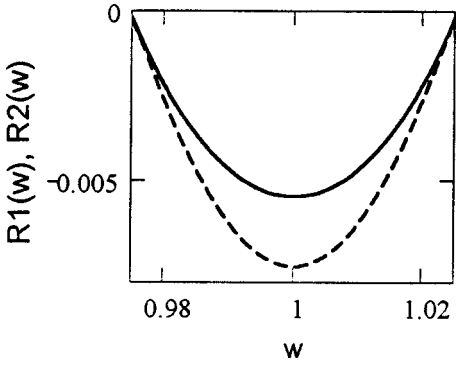

FIG. 7. Residue at fixed points on the axis ($K=1$). Solid line: $X1$, dashed line: $X2$.

(i) Equation (30) has a first obvious solution: $\psi=0$. Substituting this value into Eq. (31), and recalling that $W(0)=w$, we find

$$G(\theta,K,w,n)\equiv w-\frac{K}{(2\pi)^2}\cos 2\pi\theta-n=0, \tag{34}$$

where n is any integer, positive, zero, or negative. It will be shown below that the physically relevant value is $n=1$, which we use here. For K lying in the physical range and kept fixed, it is easily seen that Eq. (34) has a real solution only for w restricted to a finite range. Indeed, there is no such solution (with $|\cos 2\pi\theta|\leqslant 1$) as w increases from zero up to a certain minimum value w_m, for which there suddenly appears a solution: $\cos 2\pi\theta=-1$, i.e., $\theta=\frac{1}{2}$. This bifurcation point is determined by setting $G(1/2,K,w_m,1)=0$, from which we find, using Eq. (34):

$$w_m=1-(2\pi)^{-2}K. \tag{35}$$

As w is further increased, this fixed point splits into two new fixed points moving apart, one to the left and one to the right, until they reach, respectively, the values $\theta=0$ and $\theta=1$, which are physically equivalent ($1=0 \bmod 1$). This merging occurs for $w=w_M$, which defines another bifurcation point, determined by the equation $G(0,K,w_M,1)=0$, which yields

$$w_M=1+(2\pi)^{-2}K. \tag{36}$$

When w is further increased, these fixed points on the polar axis disappear.

In conclusion, *for $w_m\leqslant w\leqslant w_M$, there are two fixed points on the polar axis*: $X1=(0,\theta 1)$, $X2=(0,\theta 2)$; *their location is shown in Fig. 6 (for $K=1$). The extreme values of w are bifurcation points: for $w=w_m$ the fixed points merge at $\theta=\frac{1}{2}$, and for $w=w_M$ they merge at $\theta=0$. For w below w_m, or above w_M, these fixed points disappear.*

For the correct understanding of this result, it should be kept in mind that the polar axis $\psi=0$ is globally invariant, but its individual points are *not* fixed points, except when $K=0$. When $K>0$, and w lies in the range defined above, there remain exactly two fixed points on the axis. Note also that these points do not appear as distinct in the polar representation [such as Fig. 3(b); this feature will be further discussed in Sec. V.]

The residue at these fixed points is calculated from Eq. (33), and is plotted in Fig. 7 (for $K=1$). Both residues are negative over the whole range of allowed values of w (and also for all physical values of K), meaning that both fixed points on the axis are *unstable X points*.

Equation (34) possesses additional solutions obtained by choosing $n=0, -1, -2, \ldots$ or $n=2,3, \ldots$. One can easily convince oneself that the latter solutions exist only for values of K and w which are well beyond the physically relevant range; these solutions will no longer be discussed here.

(ii) Equation (30) also possesses solutions with $\psi\neq 0$, for which $\sin 2\pi\theta=0$. This equation is satisfied for $\theta=0$ and $\theta=\frac{1}{2}$. Substituting these values into Eq. (31) we find the following equations for ψ:

$$\theta=\frac{1}{2}: \quad F1(\psi,K,w,n)\equiv W(\psi)+\frac{K}{(2\pi)^2(1+\psi)^2}-n=0, \tag{37}$$

$$\theta=0: \quad F2(\psi,K,w,n)\equiv W(\psi)-\frac{K}{(2\pi)^2(1+\psi)^2}-n=0. \tag{38}$$

We analyze the solutions of these equations by a graphical and numerical method. We fix a value of K somewhere in the physical range, and plot the graphs of the two functions $F1$ and $F2$ for different values of the integer n.

(a) The graph of the functions $F1(\psi,K,n)$ for the typical fixed value $K=2.3$ is shown in Fig. 8 in the range $-1<\psi\leqslant 1$. The obvious property of this function, visible in Eq. (37), is the existence of a singularity at $\psi=-1$ for all K and w. For all values of n, the curves are monotonously decreasing from $+\infty$ to $-\infty$; hence they cross the axis $\psi=0$ exactly once. It follows that there exists an infinite number of roots in the range $-1<\psi<\infty$, one for each value of n. Our task is to identify the roots located in the physical domain $0\leqslant\psi\leqslant 1$.

For small values of w, there is no root in the physical domain, as can be seen in Fig. 8(a). As w is increased, the curves representing the function $F1$ are lifted upward. As a result, for a certain critical value $w=w_{C1}^{(1)}=0.941$ (for K

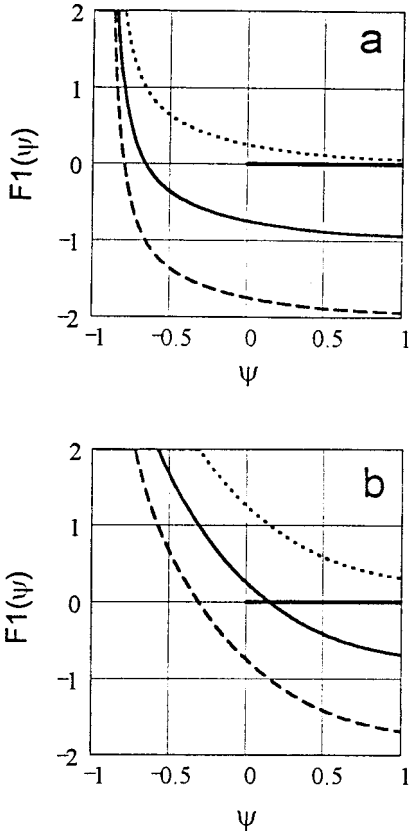

FIG. 8. The function $F1(\psi,K,w,n)$ for $K=2.3$ and two values of w. (a) $w=0.2$; (b) $w=1.2$. The three curves correspond to $n=0$ (dotted line), 1 (solid line), and 2 (dashed line). The physical range of ψ is emphasized.

$=2.3$), the curve for $n=1$ produces a root $\psi1=0$, and hence a fixed point $Y1=(\psi1,\frac{1}{2})$ in the physical domain. As w is further increased, the root $\psi1$ moves to the right [Fig. 8(b)]. Then, suddenly, when w reaches a new critical value $w_{C1}^{(2)}=1.941$, an additional root $\psi1^{(2)}$ appears in the physical domain: it is produced by the curve $n=2$. A new critical value appears at $w_{C2}^{(3)}=2.941$, with a third root $\psi1^{(3)}$ entering the physical domain ($n=3$). For still higher values of w, this pattern no longer changes; when $n=4$ produces a physical root, the root $\psi1$ ($n=1$) leaves the physical domain. Thus, for all values of $w>w_{C2}^{(3)}$, there are three roots in the relevant range.

The critical values of w depend, of course, on K. The fundamental threshold, $w=w_{C1}$, above which the first physical root appears, is obtained by expressing that the function $F1$, for $n=1$, possesses a root $\psi1=0$, corresponding to a fixed point $Y1$. From Eq. (37), we find

$$F1(0,K,w_{C1},1)\equiv w_{C1}+\frac{K}{(2\pi)^2}-1=0. \tag{39}$$

Comparing this equation with Eq. (34), we see that it is identical to the equation $G(1/2,K,w_m,1)=0$ determining the lower bifurcation point for the fixed points on the axis; hence

$$w_{C1}=w_m=1-(2\pi)^{-2}K. \tag{40}$$

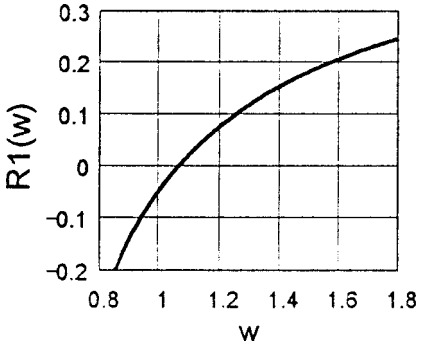

FIG. 9. Residue at the fixed point $Y1$ ($K=2.3$).

Thus, for this value of w, the two merged fixed points on axis ($X1$,$X2$) and the fixed point $Y1$ at $\theta=\frac{1}{2}$ coincide at ($\psi=0,\theta=1/2$). The stability of this fixed point is marginal [residue $R(Y1)=0$].

In Fig. 9, we plot the residue at $Y1$ (for $K=2.3$) as a function of w. We see that below the threshold $w_m=0.942$, when $\psi1<0$, the fixed point $Y1$ is hyperbolic, whereas above the threshold, when $\psi1>0$ (i.e., in the physical domain), $Y1$ is elliptic.

A second threshold which is also physically relevant is the value of $w=w_{C1}^{(2)}$ above which the root determined by $n=2$ enters the physical domain. By the same reasoning as above, we find that this second threshold is

$$w_{C1}^{(2)}=w_m+1. \tag{41}$$

Thus, *for* $w_m\leqslant w<w_m+1$, *there is exactly one elliptic fixed point* $Y1$ *within the physical domain*. The location of the fixed elliptic point $Y1$ within the physical domain, for a given K, as w is varied in the interval defined above, is shown in Fig. 10, for $K=2.3$. For reasons shown below, it appears that the situations corresponding to higher values of w, for which the function $F1$ produces two or three solutions in the physical range, are physically irrelevant, and will not be further discussed here.

(b) The graphs of the function $F2(\psi,K,w,n)$ are shown in Fig. 11 in the range $-1<\psi<1$ for $K=2.3$ and for two values of w. From Eq. (38), we see that this function also has a singularity at $\psi=-1$, but here it takes the *negative* value $F2(-1,K,w,n)=-\infty$. As a result, the shape of the curves is

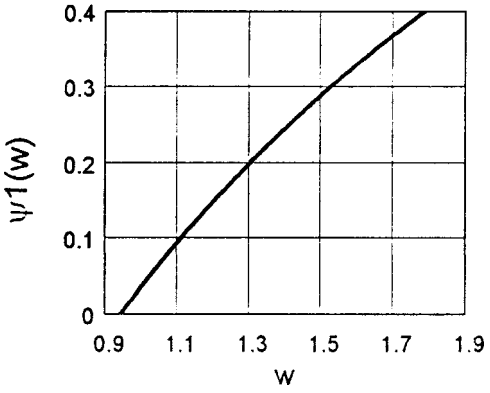

FIG. 10. Radial coordinate $\psi1(w)$ of the fixed point $Y1$ ($K=2.3$).

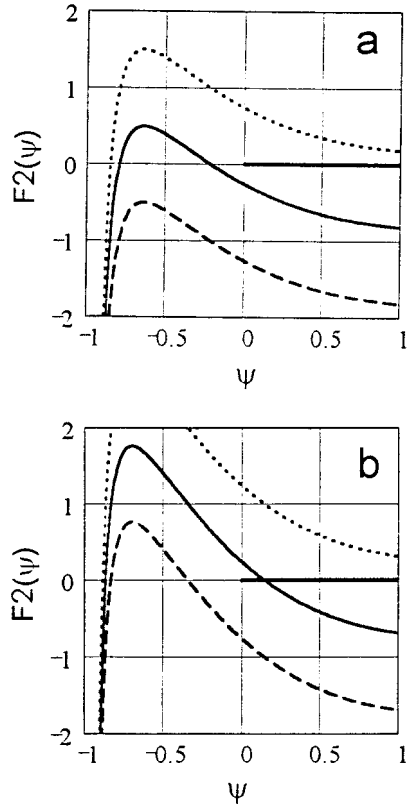

FIG. 11. The function $F2(\psi,K,w,n)$ for $K=2.3$ and two values of w: (a) $w=0.8$; (b) $w=1.3$. The three curves correspond to $n=0$ (dotted line), 1 (solid line), and 2 (dashed line). The physical range of ψ is emphasized.

quite different from $F1$ (Fig. 8): all curves have now *a maximum*. As a result, there are three possibilities, varying with n, K, and w: (1) the curve crosses the axis $\psi=0$ at two points; (2) the curve is tangent to the axis $\psi=0$; and (3) the curve does not cross the axis $\psi=0$.

For small values of w, there is again no root in the physical domain $0\leqslant\psi\leqslant 1$. As w increases, the curves move upward, and when w reaches a critical value w_{C2}, the branch $n=1$ produces a root at $\psi 2=0$ [hence a fixed point $Y2=(\psi 2,0)$]. Just as in the previous case, one readily finds that this threshold value coincides with the upper bifurcation point w_M, Eq. (36):

$$w_{C2}=w_M=1+(2\pi)^{-2}K. \tag{42}$$

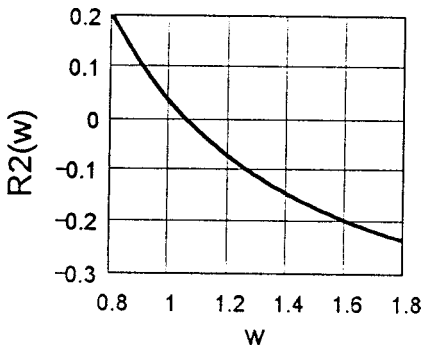

FIG. 12. Residue at the fixed point $Y2$ ($K=2.3$).

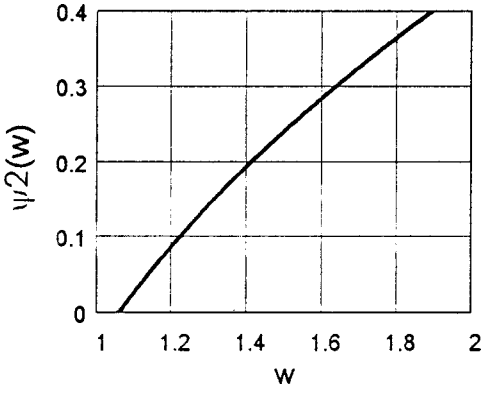

FIG. 13. Radial coordinate $\psi 2(w)$ of the fixed point $Y2$ ($K=2.3$).

The residue at $Y2$ shows that as soon as this fixed point enters the physical domain ($\psi 2>0$); i.e., at $w=w_M$ ($=1.058$ for $K=2.3$), its character changes from elliptic to hyperbolic (Fig. 12).

The equality $w_{C2}=w_M$ shows that the threshold value for $Y2$ coincides with the upper bifurcation point for $X1$ and $X2$. At this value of w the two fixed X points $X1$ and $X2$ and the former O point $Y2$ merge at the origin ($\psi=0$, $\theta=0$). For $w>w_M$, there are no longer any fixed points on the polar axis, and there remains a single X point in the physical domain, at ($\psi 2>0$, $\theta=0$). The location of $\psi 2$ as a function of w for $K=2.3$ is shown in Fig. 13.

The second threshold $w_{C2}^{(2)}$, above which a second root, for $n=2$, enters the physical domain at $\theta=0$ is: $w_{C2}^{(2)}=w_M+1$. Thus, *for* $w_M<w<w_M+1$ *there is exactly one hyperbolic fixed point* $Y2$ *at* $\theta=0$ *within the physical domain*. We do not further discuss situations in which additional fixed points appear in the physical domain.

Before summing up this discussion, it is interesting to consider the limit $K\to 0$, which is singular. Indeed, as seen from Eqs. (37) and (38), when K is strictly 0, the pole of the functions $F1$ and $F2$ no longer exists; moreover, the two functions coincide: $F1(\psi,K,w,n)=F2(\psi,K,w,n)$ (Fig. 14). The two roots $\psi 1$ and $\psi 2$ tend continuously to the common value $\psi 1(0)=\psi 2(0)=0$. (This does not mean that the two fixed points merge: they have different values of θ.) All

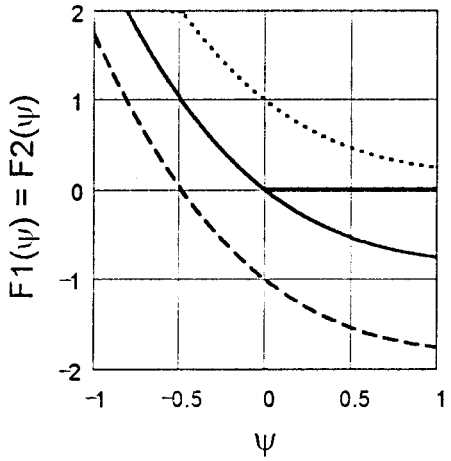

FIG. 14. The function $F1(\psi,K,w,n)=F2(\psi,K,w,n)$ for $K=0$, $w=1$, $n=0$ (dotted line), 1 (solid line), and 2 (dashed line).

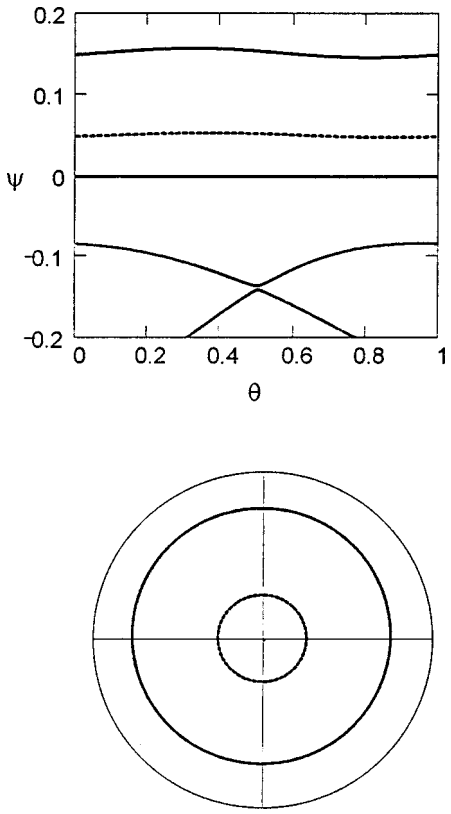

FIG. 15. Tokamap phase portrait: case I ($K=0.5$, $w=0.8$, and $N=10^3$).

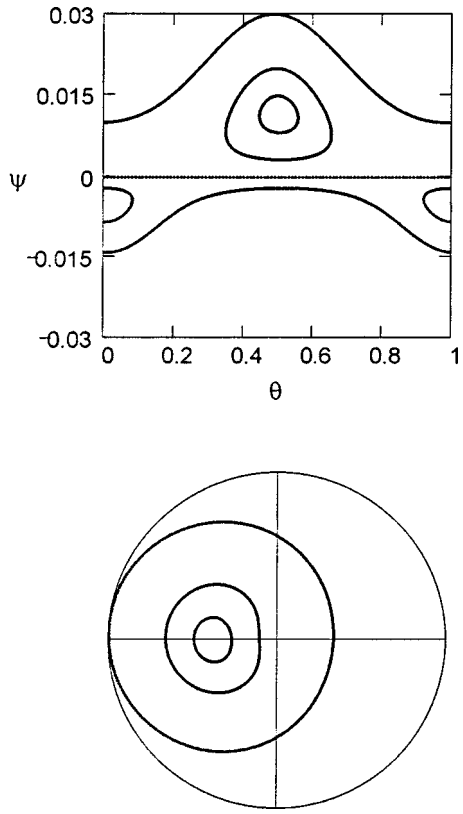

FIG. 16. Tokamap phase portrait: case II ($K=0.5$, $w=1.005$, and $N=10^3$).

curves cross the axis $\psi=0$ once; they produce positive roots outside the physical domain for $n\leqslant 0$, a zero root for $n=1$, and negative roots for $n\geqslant 2$.

V. TOPOLOGY OF TOKAMAP PHASE PORTRAITS

We now illustrate the modifications of the phase portraits in the neighborhood of the polar axis as w is progressively increased, keeping K fixed. We take for illustration a rather small value $K=0.5$, in order to have well-defined island chains and KAM surfaces (i.e., very narrow chaotic layers near X points). For clarity, we represent in the forthcoming figures only a rather narrow strip ($0\leqslant\theta<1,0\leqslant\psi<\Delta\psi$) near the polar axis; in the square representation, we sometimes also plot an extended phase portrait, including a strip in the negative ψ domain. For the chosen value $K=0.5$, we find by Eqs. (35) and (36): $w_m=0.9873$, $w_M=1.0127$.

Case I. Our first illustration (Fig. 15), $w=0.8$, corresponds to $w<w_m$. In this case *there is no fixed point in the physical domain.* As a result, there are no period-1 islands near the axis: all surfaces visible in the physical strip are represented in the square form as slightly deformed horizontal curves $\psi\approx$const>0. In the polar representation, the phase portrait in this region appears as a set of concentric circles centered on the origin. Such a picture provides a model of a *tokamak in the (rather idealized) high aspect ratio limit,* $(R/a\gg 1)$, *sometimes called the standard tokamak model* [1]. *The physical magnetic axis*—around which the magnetic surfaces are wound—*coincides in this case with the mathematical polar axis*. The fixed points are located in the negative-ψ region, where we find a ''regular'' pair of fixed points: one elliptic $Y2$, at ($\psi 2=-0.163$, $\theta 2=0$) and one hyperbolic at $Y1$ ($\psi 1=-0.139$, $\theta 1=0.5$); but these features are mathematical ''ghosts'' that are physically inaccessible. We know indeed that any orbit starting initially with a positive ψ remains forever in the positive-ψ domain.

Case II. Figure 16 ($w=1.005$) corresponds to $w_m<w<w_M$. As w increases from the value of case I, all the fixed points move upwards. The point $Y1$, which is closest to the polar axis, reaches the latter before $Y2$. At this stage, which arises when $w=w_m$, a first *bifurcation* occurs. When $w=w_m+\epsilon$ (with $\epsilon>0$), the formerly hyperbolic point $Y1$ penetrates into the physical region ($\psi 1>0$, $\theta 1=0.5$), and at the same time changes its nature from hyperbolic to elliptic. Simultaneously it gives rise to two additional hyperbolic points $X1$ and $X2$, located on the polar axis. This ''trebling'' of the fixed point $Y1$ at the bifurcation is actually required by the Poincaré-Birkhoff theorem. The bifurcation can be described in the following picturesque way. As the parameter w crosses the threshold w_m, the hyperbolic point $Y1$ ''decays'' into an elliptic point and two hyperbolic ones. This process obeys a law of ''*conservation of stability index*'': the difference between the number of elliptic points and the number of hyperbolic points remains constant as w varies. It is important to note, however, that this simple conservation rule requires that all fixed points, both physical and unphysical, be taken into account.

Figure 16 shows the appearance of the phase portrait above the first bifurcation. Here again, we must emphasize that all the features appearing in the $\psi<0$ half-space are ''ghosts,'' that are inaccessible. The polar graph corresponding to this case is also shown in Fig. 16: it is clearly struc-

tured around the fixed point $Y1$. The islands of the square graph appear in the polar graph as closed curves around $Y1$ that do not include the origin; the KAM surfaces appear as closed curves, also centered around $Y1$, but also enclosing the origin. The latter does not appear to play any major role in the organization of the structure. This shows the ambivalence of the polar axis in this problem. *Although the polar axis is globally invariant, its individual points are not fixed points*. As a result, *the origin in the polar representation is not a fixed point*. The only (physical) fixed point is the elliptic point $Y1$ ($\psi 1=0.0116$, $\theta 1=0.5$): the closed surfaces of the island as well as the KAM surfaces are centered on it. Hence, we must interpret $Y1$ as the *magnetic axis of the tokamak*. The argument in favor of this interpretation is strengthened by recalling that the main effect of a $m=1$ perturbation in a tokamak is the displacement of its magnetic axis away from the geometric polar axis (see e.g., Ref. [30], Sec. 6.4). The only remaining question is the role of the two X points $X1$ and $X2$ on the polar axis. They do not seem to play any direct role in the polar representation: they are, indeed, ''squeezed'' into the single origin. They do, however, show up in a certain ''delicate'' way, as will be seen below.

Case III. As w is further increased, it reaches the new threshold w_M, at which a second *bifurcation* takes place: its nature is, in a sense, inverse to the previous one. The two X points $X1$ and $X2$ and the O point $Y2$ now meet and merge at the origin ($\psi=0$, $\theta=0$). Above the threshold, at $w=w_M+\epsilon$, there remains a single X point, $Y2$, in the physical domain, ($\psi 2>0$, $\theta 2=0$). One may thus speak about a ''recombination'' of two X points and one O point, to yield a single X point. The rule of ''conservation of the stability index'' (hence the Poincaré-Bertrand theorem) is again satisfied. Let us stress the fact that now *both fixed points are located in the physical domain*.

The topology of the phase portrait is drastically modified. Figure 17 shows the neighborhood of the polar axis above the second bifurcation, for $w=1.05$. We now have one fixed O point $Y1$ ($\psi 1=0.179$, $\theta 1=0.5$) and one fixed X point $Y2$ ($\psi 2=0.167$, $\theta 2=0$). Around the first one there appears an *island*, within which the orbits are closed circles enclosing the fixed point. At the second point start the two branches of a separatrix, separating the island from the ''outer world.'' Above and below the separatrix there are ''passing orbits,'' i.e., KAM surfaces. The picture in the polar representation is quite interesting. The fixed O point $Y1$ is radially displaced away from the origin in the $2\pi\theta 1=\pi$ direction. The island orbits have the characteristic ''banana'' shape centered on $Y2$: this shape is quite common in tokamak physics. The separatrix appears as an ''extreme banana'' whose tips merge at the fixed X point $Y2$, displaced in the opposite direction ($\theta 2=0$) away from the origin. The KAM surfaces lying above the separatrix in the square representation are mapped into circles enclosing the separatrix (hence also the origin). The KAM barriers which are exterior to the separatrix, but lie below it in the square, are mapped into circles encircling the origin, but enclosed by the inner branch of the separatrix. This peculiar topology shows that the concepts of ''inside'' and ''outside'' are somewhat ambiguous in toroidal geometry.

The remarkable point about this type of phase portrait is

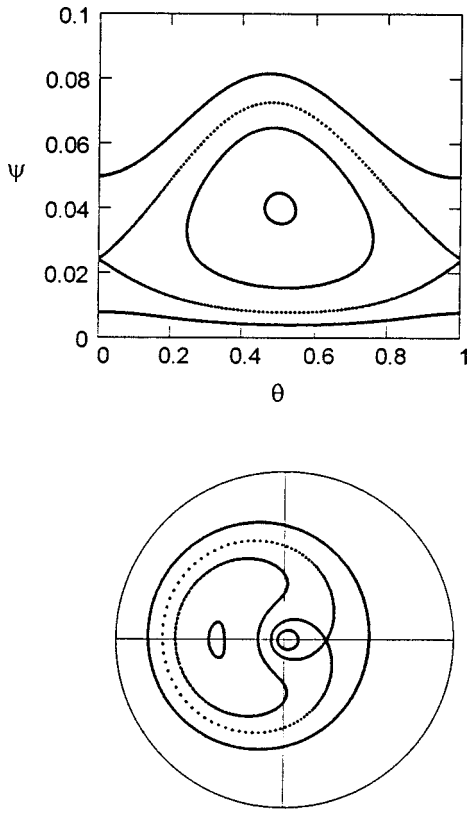

FIG. 17. Tokamap phase portrait: case III ($K=0.5$, $w=1.05$, and $N=10^3$).

that it arises during the well-known *sawtooth instability* in a real tokamak (see, e.g., Ref. [30] and Ref. [31], Sec. 7.6), and is the basis of Kadomtsev's theory of the sawteeth phenomenon. In tokamak language, it is produced by an $m=1$ instability. It appears whenever there is a region with $q<1$ (i.e., $W>1$ in our language, which requires $w>1$): this fits precisely the conditions of our case III. In the temporal sequence, this situation will be followed by a reconnection, which expels the inner bubble and restores a topology of the type of case II. Thus the tokamap is consistent with tokamak physics.

Case IV. As w continues increasing, the topology of case III is maintained, with the magnetic axis being pushed further and further away from the geometric polar axis. A new bifurcation occurs when the root $\psi 1^{(2)}$ produced by the branch $n=2$ of the function $F1$ enters the physical domain. The scenario described above for the roots $n=1$ is then repeated: a new O point appears first close to the $\psi=0$ axis at $\theta=0.5$, followed by the appearance of a second X point at $\theta=0$. In the polar representation, this implies the appearance of a second ''magnetic axis'' located ''outside'' the inner separatrix, and hence encircled by the latter; around this second axis a number of concentric KAM barriers are formed. This type of picture does not seem to be produced by any physical process in a tokamak: case IV should therefore be considered irrelevant.

As a result of this discussion, *we shall henceforth restrict the variation of w to the range* $0<w<w_m(K)+1$, *this being the range relevant to tokamak physics*. The bifurcation values w_m and w_M depend on the stochasticity parameter K. In practice, the most interesting situations are contained be-

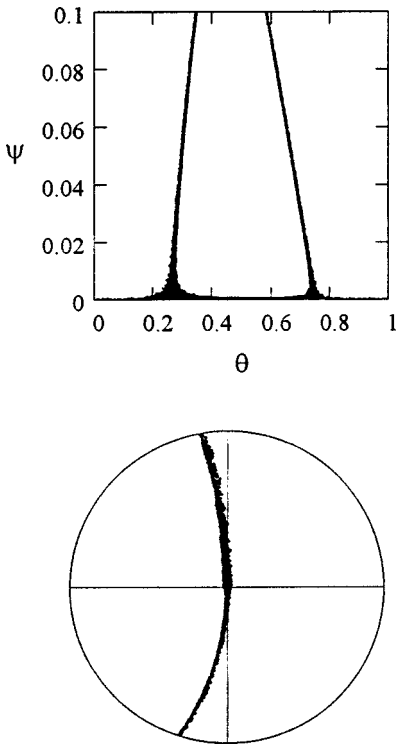

FIG. 18. Stochastic layer around the O point in the presence of X-points on the axis ($K=4.47$, $w=1$, and $N=6\times10^3$). (The radial coordinate in the polar plot is limited to $\psi=0.03$.)

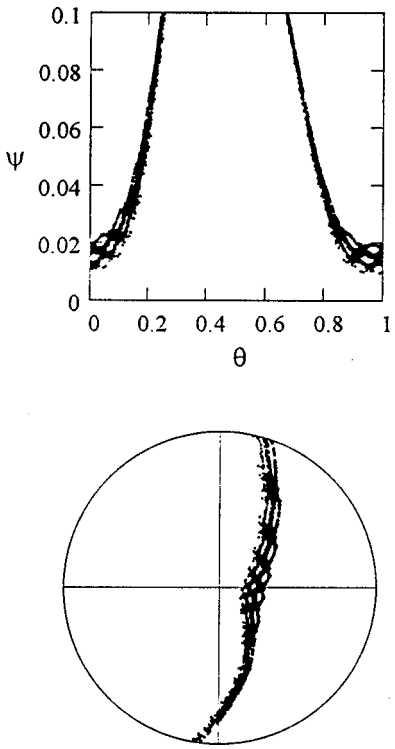

FIG. 19. Stochastic layer around the O point in the presence of a single X point off axis ($K=3.9$, $w=1.05$, and $N=6.10^3$). (The radial coordinate in the polar plot is limited to $\psi=0.07$.)

tween $w_m(K)-\Delta$ and $w_m(K)+\Delta$, where Δ is some small quantity compared to 1, thus in the neighborhood of $w=1$.

In order to complete this discussion, we make some remarks about the peculiar role of the polar axis in the tokamap. This axis is represented as a single point in the polar representation, but shows up as a segment of length 1 in the ''square'' representation. The axis could thus be thought of as being materialized by a very thin piece of wire perpendicular to the plane of section, of infinitesimally small radius, around which the various poloidal orientations are distinguishable. As was stressed repeatedly, the global invariance of the polar axis does *not* imply that each of its points is a fixed point: this is only true for $K=0$. For finite K, setting $\psi_\nu=\psi_{\nu+1}=0$ in Eq. (24) leaves us with a nontrivial one-dimensional map (which could be called ''*aximap*'') showing that, in general, any point of the axis moves at each iteration to a new poloidal position (in the polar language, this means that the point moves around the axis by a certain angle)

$$\theta_{\nu+1}=\theta_\nu+w-\frac{KA}{(2\pi)^2}\cos 2\pi\theta_\nu \pmod 1. \qquad (43)$$

This map has fixed points [for which it reduces to Eq. (34)]: for $w_m<w<w_M$, there are two fixed points $X1$ and $X2$, which we know from our previous analysis. These points do not seem to play any special role in the polar representation of Fig. 16; they are squeezed into the origin.

There is, however, one way of making their presence manifest, even in the polar representation. We recall that for sufficiently high K, a chaotic layer develops around each island chain; it grows thicker as K increases, up to the final destruction of the island chain. This stochastic layer always starts in the neighbourhood of the X points of the separatrix encircling the islands: they are the most ''fragile'' points of the chain [32]. With these facts in mind, we consider the phase portrait of the tokamap in the neighborhood of the polar axis for $K=4.47$ and $w=1$ (Fig. 18). (Note that we have to take a rather large value of K in order to see anything; we know, indeed, that the region near the axis is very robust to perturbations.) In this case the stochastic layer starts near the points $X1$ and $X2$, as appears clearly in the square representation. In the polar representation, we see that the corresponding orbit is thickest in the angular sectors $2\pi\theta\approx\pi/2$, $3\pi/2$. The X points thus determine the starting *direction* of the stochastic layer.

Consider next the case $K=3.9$ and $w=1.05$: this is a case III situation, where there are no X points on the polar axis; there is only one X point off-axis (Fig. 19). Here the chaotic layer starts near the X point: in the polar diagram the layer is thickest in the $\theta=0$ direction, contrary to the previous case.

We may note, upon looking at Figs. 18 and 19 that w has another important effect on the dynamics. *A larger w implies a lower stochasticity threshold*. Indeed, the chaotic layer in the nearby regions of the phase space is more strongly developed at $K=3.9$ for $w=1.05$ than at the larger value of $K=4.45$, for $w=1$. Thus, increasing w [i.e., decreasing $q(0)$] has a destabilizing effect on the magnetic field configuration. This is again in agreement with standard tokamak physics.

VI. TOKAMAP AND CONTINUOUS TIME RANDOM WALK

A quite different type of information about the tokamap dynamics is obtained by a consideration of *time series*, in

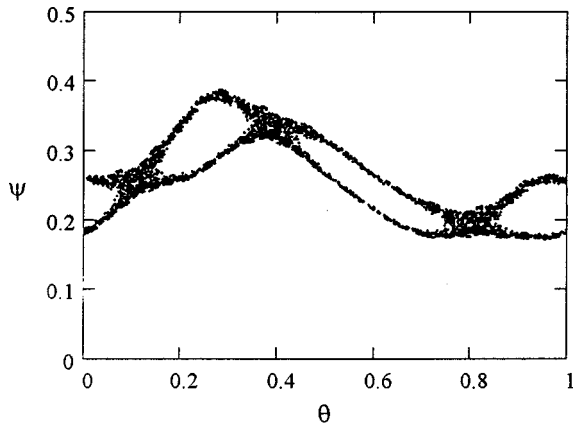

FIG. 20. Stochastic orbit around a three-island chain ($K=3.7$, $w=1$, and $N=3\times10^3$).

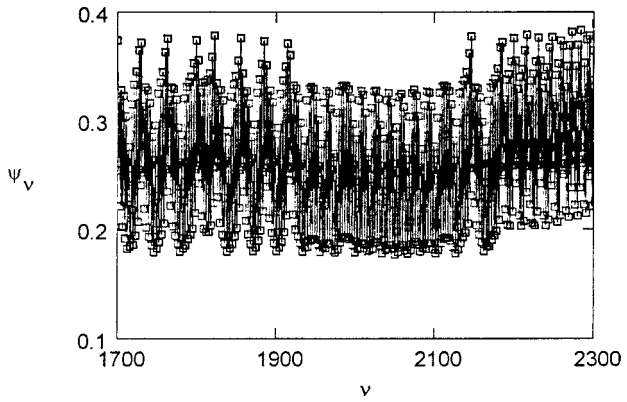

FIG. 21. Time series for the stochastic orbit of Fig. 20.

particular graphs of ψ_ν vs ν. It is in this representation that a very important aspect of the evolution of incompletely chaotic systems is manifest: *stickiness*. A chaotic orbit spends a long time near the boundaries of island chains, KAM barriers and cantori. This property is due to the ''braking'' action of the complex fractal structure of these boundaries (islands, around islands, around islands, etc.). Rather than going into a detailed description of these extremely complicated processes, we take a rather different point of view in the approach of this problem: we try to establish a ''coarse grained'' picture which eventually leads to ''macroscopic'' equations of evolution. This methodology was developed in a previous study of the standard map [33]. It started from the observation that a graph of the successive iterations of the radial coordinate presents rather regular oscillations in a certain ''basin,'' followed by a sudden jump to another mode of oscillation in a different basin, which goes on for a certain time till another jump happens, etc. We show here that this type of behavior is generic.

We consider, for $K=3.7$ and $w=1$, a chaotic orbit starting at $\psi_0=0.20$ and $\theta_0=0.80$: this orbit remains confined in a region blocked by two KAM barriers below and above a three-island chain (around $W=\frac{2}{3}$), as seen in the phase portrait of Fig. 20.

In Fig. 21, we see a typical section of the time series (ψ_ν vs ν) of this orbit, for $1700<\nu<2300$. The behavior described above is manifest: three basins can be identified from three regimes of oscillation (mean position, amplitude, and frequency). They correspond to motion encircling the island chain (basin O, $1700<\nu<1910$), motion below the islands (basin L, $1910<\nu<2110$) and motion above the islands (basin H, $2200<\nu<2400$).

This behavior is exactly analogous to the one seen in the standard map [33,34]. It can be described by a *continuous time random walk*. The orbit is then globally described by a particle sojourning in a basin for a certain time, making a transition to another basin, sojourning there, making another jump, etc. The process is completely defined by prescribing a *waiting time probability distribution* in basin m: $p_m(\zeta)$, and a transition probability from basin m to basin n: f_{nm}. (We recall that the role of time is played here by the toroidal coordinate ζ). Both quantities can be determined by an analysis of long time series. Using then standard techniques of random walk theory, the probability density of finding the particle in basin m at time ζ, $n_m(\zeta)$ can be found exactly.

We do not describe here in detail the development of these ideas: the methodology is exactly the same as in Refs. [33–35], and the conclusion is identical. The magnetic field line ''diffusion'' is a typical example of ''*strange transport*:'' the effective running diffusion coefficient decays asymptotically to zero as an inverse power law. This behavior is characteristic of the dynamics in an *incompletely chaotic regime*, in which the motion is bounded by upper and lower KAM barriers. We checked all these properties successfully on the tokamap; our simulations are, however, not yet sufficiently extensive in order to provide reliable quantitative results. This specific problem will be addressed in forthcoming work.

VII. CONCLUSIONS

We have shown that a simple Hamiltonian map can be constructed, fulfilling the minimum requirements for a representation of a magnetic field in toroidal geometry. In the present paper we considered only the situations in which there exists a monotonous profile of winding number (or of safety factor). This tokamap describes a structure that is very robust in the central region, the global stochasticity starting (for increasing K) in the edge region: the map could therefore prove useful as a model of a tokamak with an ergodic divertor. The central region has some quite interesting topological features, which can change dramatically (including bifurcations) as the value of the safety factor on axis is varied. Typical configurations known from tokamak physics are qualitatively reproduced by the map.

Many more properties of the tokamap will be studied in forthcoming works. These include questions such as the influence of the shape of the winding number profile, the dependence on the parameters of various physical properties, similarity and scaling properties. Last but not least, we intend to put charged particles in this magnetic field and study the transport properties in a partially chaotic tokamak configuration. This problem, which is very poorly understood, is of crucial importance for fusion physics.

ACKNOWLEDGMENTS

Useful discussions with J. H. Misguich, Y. Elskens, and R. B. White are gratefully acknowledged.

[1] R. Balescu, *Transport Processes in Plasmas* (North-Holland, Amsterdam, 1988).
[2] F. L. Hinton and R. D. Hazeltine, Rev. Mod. Phys. **48**, 239 (1976).
[3] A. H. Boozer, Phys. Fluids **27**, 2055 (1984).
[4] D. W. Kerst, J. Nucl. Energy, Part C **4**, 253 (1962).
[5] J. R. Cary and R. G. Littlejohn, Ann. Phys. (N.Y.) **151**, 1 (1983).
[6] A. Salat, Z. Naturforsch. Teil A **40**, 959 (1985).
[7] K. Elsässer, Plasma Phys. Controlled Fusion **28**, 1743 (1986).
[8] H. Wobig, Z. Naturforsch. Teil A **42**, 1054 (1987).
[9] A. H. Boozer and R. B. White, Phys. Rev. Lett. **49**, 786 (1982).
[10] R. B. White, in *Statistical Physics and Chaos in Fusion Plasmas*, edited by W. Horton and L. Reichl (Wiley, New York, 1984).
[11] D. F. Düchs, A. Montvai, and C. Sack, Plasma Phys. Controlled Fusion **33**, 919 (1991).
[12] T. J. Martin and J. B. Taylor, Plasma Phys. Controlled Fusion **26**, 321 (1984).
[13] A. Punjabi, A. Verma, and A. Boozer, Phys. Rev. Lett. **69**, 3322 (1992).
[14] A. Punjabi, A. Verma, and A. Boozer, J. Plasma Phys. **52**, 91 (1994).
[15] A. Punjabi, H. Ali, and A. Boozer, Phys. Plasmas **4**, 337 (1997).
[16] S. S. Abdullaev and G. M. Zaslavsky, Phys. Plasmas **2**, 4533 (1995).
[17] S. S. Abdullaev and G. M. Zaslavsky, Phys. Plasmas **3**, 516 (1996).
[18] S. S. Abdullaev, K. H. Finken, A. Kaleck, and K. H. Spatschek, Phys. Plasmas **5**, 196 (1998).
[19] J. T. Mendonça, Phys. Fluids B **3**, 87 (1991).
[20] H. Goldstein, *Classical Mechanics*, 2nd ed. (Addison-Wesley, New York, 1980).
[21] E. Ott, *Chaos in Dynamical Systems* (Cambridge University Press, Cambridge, 1993).
[22] B. Chirikov, Phys. Rep. **52**, 265 (1979).
[23] A. J. Lichtenberg and M. A. Lieberman, *Regular and Stochastic Motion* (Springer, Berlin, 1983).
[24] J. H. Misguich and B. Weyssow, Euratom–CEA Internal Report No. NTΦ 8, 1989.
[25] J. M. Greene, J. Math. Phys. **20**, 1183 (1979).
[26] R. S. MacKay, J. D. Meiss, and I. C. Percival, Physica D **13**, 55 (1984).
[27] D. Bensimon and L. P. Kadanoff, Physica D **13**, 82 (1984).
[28] R. S. MacKay, *Renormalisation in Area-Preserving Maps* (World Scientific, Singapore, 1993).
[29] R. S. MacKay and J. Stark, Nonlinearity **5**, 867 (1992).
[30] J. Wesson, *Tokamaks* (Clarendon, Oxford, 1987).
[31] B. B. Kadomtsev, *Tokamak Plasma, a Complex Physical System* (Institute of Physics and Physical Society, Bristol, 1992).
[32] G. M. Zaslavsky, *Chaos in Dynamic Systems* (Harwood, Chur, Switzerland, 1985).
[33] R. Balescu, Phys. Rev. E **55**, 2465 (1997).
[34] R. Balescu, *Statistical Dynamics: Matter Out of Equilibrium* (Imperial College Press, London, 1997).
[35] J. Misguich, J. D. Reuss, Y. Elskens, and R. Balescu, Chaos **8**, 248 (1998).